The Astrophysical Journal Letters, 888:L21 (12pp), 2020 January 10 https://doi.org/10.3847/2041-8213/ab61ff

Is π Men c's Atmosphere Hydrogen-dominated? Insights from a Non-detection of H I Lyα Absorption

A. García Muñoz[1], A. Youngblood[2,3], L. Fossati[4], D. Gandolfi[5], J. Cabrera[6], and H. Rauer[1,6,7]
[1] Zentrum für Astronomie und Astrophysik, Technische Universität Berlin, Hardenbergstrasse 36, D-10623, Berlin, Germany
garciamunoz@astro.physik.tu-berlin.de, tonhingm@gmail.com
[2] NASA Goddard Space Flight Center, Greenbelt, MD 20771, USA
[3] Laboratory for Atmospheric and Space Physics, 1234 Innovation Drive, Boulder, CO 80303, USA
[4] Space Research Institute, Austrian Academy of Sciences, Schmiedlstrasse 6, A-8042 Graz, Austria
[5] Dipartimento di Fisica, Università degli Studi di Torino, via Pietro Giuria 1, I-10125, Torino, Italy
[6] Deutsches Zentrum für Luft- und Raumfahrt, Institut für Planetenforschung, D-12489 Berlin, Germany
[7] Institute of Geological Sciences, Freie Universität Berlin, Malteserstrasse 74-100, D-12249, Berlin, Germany
Received 2019 November 1; revised 2019 December 11; accepted 2019 December 12; published 2020 January 9

Abstract

Constraining the composition of super-Earth-to-sub-Neptune-sized planets is a priority in order to understand the processes of planetary formation and evolution. π Men c represents a unique target for the atmospheric and compositional characterization of such planets because it is strongly irradiated and its bulk density is consistent with abundant H_2O. We searched for hydrogen from photodissociating H_2/H_2O in π Men c's upper atmosphere through H I Lyα transmission spectroscopy with the *Hubble Space Telescope*'s Space Telescope Imaging Spectrograph, but did not detect it. We set 1σ (3σ) upper limits for the effective planet-to-star size ratio $R_{\mathrm{Ly}\alpha}/R_\star = 0.13$ (0.24) and 0.12 (0.20) at velocities $[-215, -91]$ km s^{-1} and $[+57, +180]$ km s^{-1}, respectively. We reconstructed the stellar spectrum, and estimate that π Men c receives about 1350 erg cm^{-2} s^{-1} of 5–912 Å energy, enough to cause rapid atmospheric escape. An interesting scenario to explain the non-detection is that π Men c's atmosphere is dominated by H_2O or other heavy molecules rather than H_2/He. According to our models, abundant oxygen results in less extended atmospheres, which transition from neutral to ionized hydrogen closer to the planet. We compare our non-detection to other detection attempts, and tentatively identify two behaviors: planets with densities $\lesssim$2 g cm^{-3} (and likely hydrogen-dominated atmospheres) result in H I Lyα absorption, whereas planets with densities $\gtrsim$3 g cm^{-3} (and plausibly non-hydrogen-dominated atmospheres) do not result in measurable absorption. Investigating a sample of strongly irradiated sub-Neptunes may provide some statistical confirmation if it is shown that they do not generally develop extended atmospheres.

Unified Astronomy Thesaurus concepts: Exoplanet atmospheres (487); Aeronomy (22); Ultraviolet astronomy (1736); Exoplanet atmospheric composition (2021)

1. Introduction

Planets in the super-Earth-to-sub-Neptune size range (radii $1 < R_p/R_\oplus < 3.8$) are not represented in our solar system but are numerous around other stars (Batalha 2014; Marcy et al. 2014). Yet, key aspects such as their composition or the mechanisms controlling their formation and evolution remain unclear. This range of sizes overlaps with the transition between rocky planets and planets with large amounts of gases and astrophysical ices (Valencia et al. 2013; Rogers 2015). Understanding this transition is critical for forming the big picture of exoplanets, and as a preparatory step to investigate planets with conditions that are apt for life. Determining the atmospheric composition of a sample of small exoplanets will prove useful to address these and other open questions in exoplanetary science. As small exoplanets are notoriously difficult to characterize, space missions such as the *CHaracterising ExOPlanets Satellite* (*CHEOPS*; Fortier et al. 2014), the Transiting Exoplanet Survey Satellite (*TESS*; Ricker et al. 2015), and the *PLAnetary Transits and Oscillations of stars* (*PLATO*; Rauer et al. 2014) will play a key role at finding the most favorable targets around nearby stars for follow-up investigations.

π Men is a quiet G0 V star of V-mag = 5.65 at 18.28 pc (Gaia Collaboration et al. 2018) orbited by two substellar objects. π Men b is a massive ($M_p/M_J \sim 10$) object on an eccentric ($e \sim 0.6$), long-period ($P_{orb} \sim 2100$ days) orbit discovered by radial velocity (Jones et al. 2002). π Men c, a small ($M_p/M_\oplus = 4.52 \pm 0.81$; $R_p/R_\oplus = 2.06 \pm 0.03$), close-in ($P_{orb} = 6.27$ days) planet (Gandolfi et al. 2018), was recently discovered using transit photometry with *TESS* (Gandolfi et al. 2018; Huang et al. 2018). Its bulk density ($\rho_p = 2.82 \pm 0.53$ g cm^{-3}) places it in a region of the mass–radius diagram consistent with a variety of compositions ranging from 100% water to a rocky core surrounded by small amounts by mass of hydrogen-helium. Interestingly, the planet sits near the radius gap ($R_{gap}/R_\oplus \sim 1.8$) of small, close-in planets (Fulton et al. 2017; Van Eylen et al. 2018) that separates the planets that are thought to have retained an atmosphere ($R_p/R_{gap} > 1$) from those that lost it as a result of irradiation-driven escape ($R_p/R_{gap} < 1$; Lopez & Fortney 2013; Owen & Wu 2013). These arguments strongly suggest that π Men c has an atmosphere that is currently escaping.

We report the first attempt to detect π Men c's upper atmosphere with *Hubble Space Telescope* (*HST*) observations of H I Lyα absorption. The search is motivated by the planet's bulk density, consistent with large amounts of hydrogen in the form of H_2 or H_2O. Under the effects of strong stellar irradiation, photodissociation of both molecules will produce H atoms that will escape the planet and form a potentially detectable extended atmosphere. The same strategy has revealed the occurrence of significant H I Lyα absorption in the atmospheres of the hot Jupiters HD 209458 b and HD 189733 b (Vidal-Madjar et al. 2003, 2004; Ben-Jaffel 2007, 2008;

Table 1
Data Sources for the Constructed 5 Å–2.5 μm Spectrum of π Men

Wavelength Range (Å)	Data Source	Scale Factor
5–124	(a)	3.3×
124–912	(a)	2×
912–1143	(a)	…
1143-1438[a]	(b)	…
1212–1220	(c)	…
1280–1320	(a)	…
1438–3000	(d)	0.47×
3000–25,000	(e)	2×10^{-11}

Notes. (a) The solar minimum spectrum from Woods et al. (2009), scaled in the X-ray to match predictions from King et al. (2019), scaled in the extreme ultraviolet (EUV; 124–912 Å) to match an average of the predictions from King et al. (2019) and France et al. (2018), and not scaled in the far ultraviolet (FUV) based on excellent agreement with the blue end of the Cosmic Origins Spectrograph (COS) spectrum (b). (b) The archival COS spectra from France et al. (2018), no scaling necessary. (c) The Lyα reconstruction from this work, shifted slightly to match the flux of the surrounding COS spectrum. (d) The archival Space Telescope Imaging Spectrograph (STIS) spectrum of the G0V star HD 39587 from Ayres (2010), scaled down to match the red edge of the COS spectrum. (e) A G0V radiative equilibrium model from Pickles (1998), scaled to match π Men's optical photometry.
[a] Except for Lyα (1212–1220 Å) and the COS detector gap (1280–1320 Å).

Lecavelier des Etangs et al. 2010, 2012; Bourrier et al. 2013), and the warm Neptunes GJ 436 b and GJ 3470 b (Kulow et al. 2014; Ehrenreich et al. 2015; Bourrier et al. 2018). The attempts to detect H I Lyα absorption around smaller and/or less irradiated planets have so far resulted in non-detections or in less clear conclusions: HD 97658 b (Bourrier et al. 2017c), 55 Cancri e (Ehrenreich et al. 2012), TRAPPIST-1 b and c (Bourrier et al. 2017a, 2017d), Kepler-444A e and f (Bourrier et al. 2017b), and GJ 1132 b (Waalkes et al. 2019). The theoretical understanding of when planets develop extended atmospheres is imperfect, and in particular the role played by atmospheric composition remains poorly explored.

2. Reconstructed Spectrum of π Men

Our hydrodynamic-photochemical model, which is the basis for the interpretation of the reported observations (see below), requires a realistic stellar spectrum as input into the top of the atmosphere. To this end, we constructed a complete 5 Å–2.5 μm spectrum for π Men from new and archival data, scaled solar spectra, and a radiative equilibrium stellar model. Table 1 gives the source for each part of the reference spectrum including any scaling factors used. The left panel of Figure 1 shows the representative spectrum of π Men as observed from Earth. In the rest of this section we describe the reconstruction of the Lyα line, which is based on new data from this work obtained to search for a planetary transit signature.

We observed π Men on 2019 July 24 during 5 consecutive orbits with the *HST* Space Telescope Imaging Spectrograph (STIS) as part of *HST*-GO-15699. The first two orbits occurred during pre-transit, the following two during transit, and the final orbit occurred post-transit, with respect to the transit observed by *TESS*. Our data were taken with the G140M grating centered at 1222 Å and the $52 \times 0\farcs2$ slit, in time-tag mode. The complete spectral range covered by each spectrum is 1194–1249 Å. We downloaded from the MAST archive the data calibrated and extracted by *calstis*.[8]

To reconstruct the bright H I Lyα line (1216 Å) from the STIS spectrum, we used methods described in Youngblood et al. (2016) to simultaneously fit a model of the interstellar medium (ISM) H I and D I absorption and a model of the intrinsic stellar emission. Given the non-detection of the planetary transit (see below), we co-added the spectra obtained in each of the five *HST* orbits for improved signal-to-noise ratio (S/N). In contrast to the procedure described in Youngblood et al. (2016), we assumed a Voigt profile for the intrinsic stellar emission, and a small Gaussian in absorption to account for the self-reversal of the line expected in G dwarfs like π Men. We find an intrinsic Lyα flux of $F(\mathrm{Ly}\alpha) = 3.80 \pm 0.40 \times 10^{-13}$ erg cm^{-2} s^{-1}. The right panel of Figure 1 shows the reconstruction compared to the STIS data. For the ISM, the best-fitting parameters are $\log N(\mathrm{H\,I}) = 18.51 \pm 0.02$ cm^{-2}, $b = 12.5 \pm 0.7$ km s^{-1}, and $v_{\mathrm{H\,I}} = -7.4^{+0.7}_{-0.8}$ km s^{-1}. Accounting for a systemic offset of -7.25 km s^{-1} in the STIS wavelength solution, we find that our fitted stellar radial velocity ($+3.48^{+0.76}_{-0.74}$ km s^{-1}) and ISM radial velocity ($-7.4^{+0.7}_{-0.8}$ km s^{-1}) agree well with measurements from *Gaia* data release 2 (DR2; Gaia Collaboration et al. 2018; $+10.73$ km s^{-1}) and predictions from the ISM Kinematic Calculator from Redfield & Linsky (2008; G and Vel clouds have velocities of -2.26 ± 1.29 km s^{-1} and $+2.28 \pm 0.76$ km s^{-1}, respectively).

We note that the Lyα flux levels detected in our STIS spectrum are less than expected, because of the unknown ISM H I column density, Doppler broadening parameter, and radial velocity at the time of planning these observations. The relative velocity between the ISM absorption and stellar emission is -11 km s^{-1}, which inconveniently makes the blue wing of the observed Lyα profile, where the strongest escaping atmosphere signatures are expected, more strongly attenuated than the red wing. Also, our fitted H I column density, while not atypical for a star at 18 pc, is on the upper end of the expected range. A priori knowledge of the ISM column density as a function of celestial coordinates would be helpful in planning exoplanet transit observations using ISM-affected lines as a backlight. For reference, Figure 7 in Appendix A compares the Lyα line of π Men with the G dwarfs HD 97334 and HD 39587 after scaling to match π Men's distance and chromospheric activity level.

Before incorporation in the analysis below, the representative 5 Å-2.5 μm spectrum is binned to a constant 1 Å. We accounted for the varying spectral resolutions of our data sources by convolving higher-resolution data with a Gaussian kernel until overlapping spectral features matched. The X-ray +extreme ultraviolet (EUV) (5–912 Å) stellar spectrum is particularly important to drive the atmospheric escape, as both hydrogen and oxygen atoms absorb at these wavelengths. Our reconstruction leads to a stellar irradiation of π Men c at these wavelengths of 1350 erg cm^{-2} s^{-1}.

To test the impact of some of the above choices on the atmospheric modeling of π Men c, we additionally produced two alternative reconstructed spectra. We refer to them as the *high* and *low* stellar spectra, because they bracket the integrated EUV flux of our reference implementation. The X-ray+EUV flux at the planet's orbital distance for the *high* spectrum is 1810 erg cm^{-2} s^{-1}, as in King et al. (2019), whereas for the *low* spectrum the flux is 1060 erg cm^{-2} s^{-1}, based on the estimates by France et al. (2018). The discrepancy between these two

[8] http://www.stsci.edu/hst/stis/software/analyzing/calibration/pipe_soft_hist/intro.html

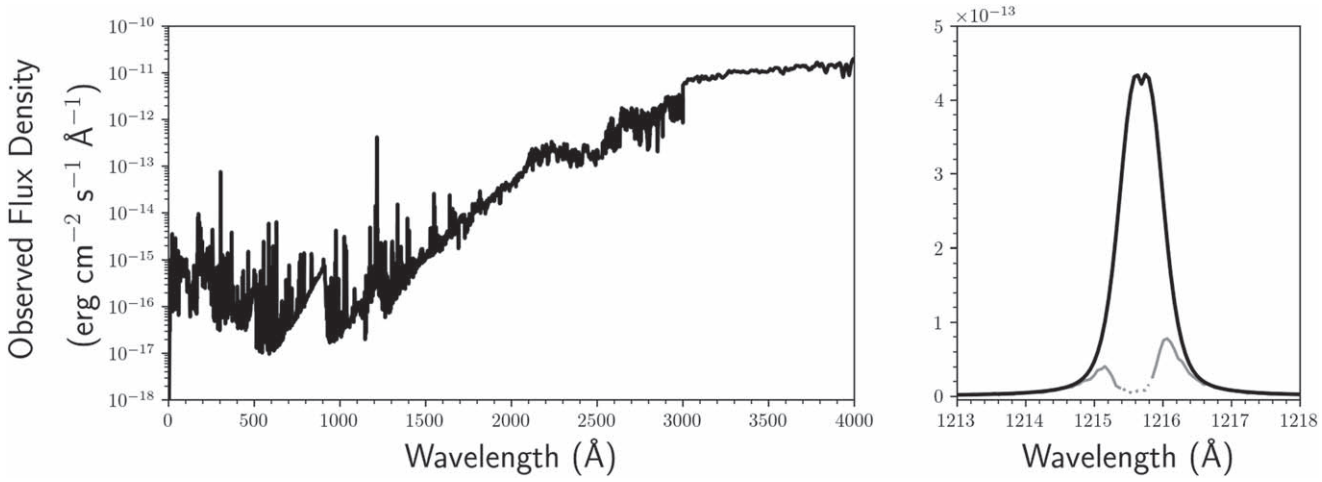

Figure 1. Left panel: the reconstructed 5–4000 Å spectrum of π Men is shown here as would be observed at 18.28 pc. Right panel: the co-added STIS G140M spectrum is shown in gray and the reconstructed intrinsic Lyα profile is shown in black, convolved to the instrument spectral resolution. The dotted line shows the geocoronal airglow-contaminated region.

works' EUV estimates occur because π Men is observed to have similar chromospheric emission to the Sun (France et al. 2018), but 3.3× higher coronal emission than the Sun (King et al. 2019). Coronal and chromospheric emission both contribute to the unobserved EUV spectral range.

3. Search for Transit of π Men c

A visual inspection of the extracted and calibrated STIS Lyα fluxes indicates that there is no clear planetary absorption signature, both in the red and blue line wings (Figure 2, left panel); fluxes obtained between −90 and +35 km s^{-1} from the line center are strongly affected by ISM absorption and geocoronal airglow emission. Before performing a deeper analysis and eventually assigning upper limits on the non-detection, it is necessary to look for and correct for the breathing effect, which is known to affect most STIS observations obtained with a narrow slit (e.g., Ehrenreich et al. 2015; Bourrier et al. 2018). We assume that the amplitude of the breathing effect is a function of the *HST* orbital phase and that it is repeatable across the five *HST* observations. We downloaded from MAST the calibrated two-dimensional spectra providing information on the photon arrival time ("_tag.fits" files) and split each *HST* observation in five sub-exposures of equal exposure time. From each sub-exposure image, we extracted the stellar spectra using a slanted extraction box with an aperture of 20 pixels and the background employing an identical extraction box, but shifted upward by 100 pixels (see Figure 8 in Appendix B). We then removed the relative background from the stellar spectra, phased each sub-exposure with *HST*'s orbit, and finally looked for repeatable trends in the fluxes integrated between +35 and +300 km s^{-1}, which is the region of the observed Lyα line with the highest flux, thus highest signal-to-noise. For the analysis of the breathing effect, we considered just the observations obtained in the second, fourth, and fifth *HST* observation because the first *HST* orbit is notoriously affected by additional systematics and the third observation has been partially obtained during the planetary ingress. We modeled the breathing effect as a polynomial of varying order, selecting the one that minimizes the Bayesian Information Criterion: BIC $= \chi^2 + k \log N$, where k is the number of free parameters and N is the number of data points. We finally obtained that the breathing effect is best described by a first order polynomial (Figure 2, top-right panel).

We applied the same correction for the breathing effect to the whole Lyα fluxes and looked for the planetary transit signature in the light curves obtained from integrating across the blue (−250 to −100 km s^{-1}) and red (+35 to +300 km s^{-1}) line wings, without finding any (Figure 2, bottom-right panel). We place an upper limit on the size of the planet's H I atmosphere by fitting a transit model of an opaque sphere to the Lyα light curve using an Markov Chain Monte Carlo (MCMC) technique. We use the `batman` package (Kreidberg 2015) with transit parameters from Gandolfi et al. (2018), and uniform limb darkening parameters. We find 1σ, 2σ, and 3σ upper limits to the size of the planet at Lyα relative to the star $R_{\mathrm{Ly}\alpha}/R_\star = 0.13$, 0.19, and 0.24 in the [−215, −91] km s^{-1} velocity range. Similarly, we find 1σ, 2σ, and 3σ upper limits in the [+57, +180] km s^{-1} range of 0.12, 0.16, and 0.20.

4. Model-based Interpretation

We built a model of π Men c's upper atmosphere to aid in the interpretation of the H I Lyα observations. It adds to the existing literature on hydrodynamic-photochemical models for solar system terrestrial planets (e.g., Kasting & Pollack 1983; Zahnle & Kasting 1986; Chassefière 1996; Tian et al. 2008) and to recent investigations of CO_2- and H_2O-rich exoplanets (e.g., Tian 2009; Johnstone et al. 2018; Guo 2019). The model solves the hydrodynamics equations for the escaping atmosphere considering photochemistry at pressures $p \lesssim 1$ dyn cm^{-2} (=1 μbar, which defines the model's lower boundary) and radial distances from the planet center $r/R_\mathrm{p} = 1$–10. Our methods build upon published work for hot Jupiters and ultra-hot Jupiters (García Muñoz 2007b; García Muñoz & Schneider 2019). The baseline scenario is an atmosphere whose bulk composition is dominated by H_2/H_2O. Although other compositions that include C-bearing gases such as CO, CO_2, and CH_4 are certainly possible, we refer to the literature (e.g., Tian 2009; Johnstone et al. 2018) and leave for follow-up work the investigation of more complex hydrogen–oxygen–carbon compositions. Our hydrogen–oxygen chemical network includes the neutrals H_2, H, H_2O, OH, O, O_2; the ions H_2^+, H^+, H_3^+, H_2O^+, H_3O^+, OH^+, O^+, O_2^+; and electrons. They participate in 79 processes, including 14 for photodissociation/-ionization (García Muñoz et al. 2005;

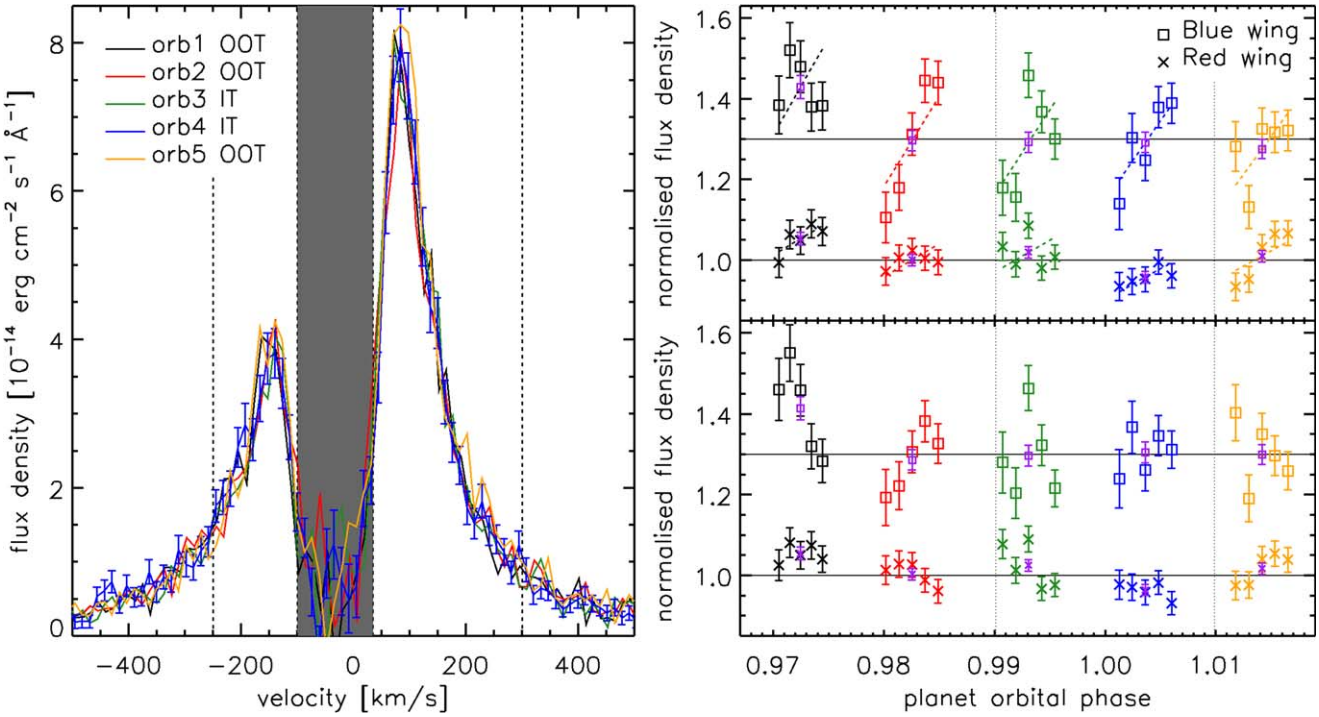

Figure 2. Left panel: comparison between the *calstis* extracted and calibrated Lyα spectra of π Men obtained for each of the five *HST* observations (orbits). The first, second, and fifth *HST* observations were conducted out-of-transit (OOT), while the third and fourth were in-transit (IT). For clarity, the uncertainties have been drawn just for the fourth observation. The gray shaded area indicates the spectral region excluded from the analysis, because heavily contaminated by ISM absorption and geocoronal airglow emission. The dashed vertical lines mark the spectral regions in the blue and red wings considered for the analysis. Top-right panel: Lyα light curve obtained integrating across the blue (square; -250 to -100 km s^{-1}; rigidly shifted upward by 0.3) and red (cross; $+35$ to $+300$ km s^{-1}) wings before correcting for the breathing effect. Colors are as in the left panel and the purple symbols indicate the average for each *HST* observation. The polynomials (straight lines) used to correct for the breathing effect are shown by dashed lines. The black horizontal lines show the modeled *TESS* transit light curve; its shape (transit depth $\sim 3 \times 10^{-4}$) is not discernible at the scale of the graph. Bottom-right panel: same as the top-right panel, but after correcting for the breathing effect. No planetary absorption signal is detected.

García Muñoz 2007a, 2007b). The energy equation includes the usual terms for advection of total enthalpy (including chemical internal energy), thermal conduction, diffusive transport of enthalpy and gravitational work. It also includes radiative contributions from deposition of stellar X-ray-EUV-FUV energy by absorption of neutrals, H_3^+ cooling in the infrared (IR; Miller et al. 2013), Lyα emission excited by electron collisions with hydrogen (Black 1981), O(^3P) emission at 63 and 147 μm (Bates 1951; Banks & Kockarts 1973), and H_2O and OH cooling through IR rovibrational bands (Hollenbach & McKee 1979). We do not solve the problem of diffuse radiation and, as an upper limit to the energy radiated away by the gas, it is assumed that all photons from the recombinations $H^+ + e \rightarrow H + h\nu$ and $O^+ + e \rightarrow O + h\nu$ are lost. We avoid prescribing efficiencies in the conversion from deposited stellar energy to actual atmospheric heating. The model aims to explore how the mass loss rate varies with the bulk atmospheric composition, and predict the gas velocities in the upper atmosphere and the prevalent form for each atom.

π Men c's bulk composition is very uncertain. Thus we consider a variety of compositions for the planet's lower atmosphere that enter into our model as boundary conditions at the $p = 1$ dyn cm^{-2} level. Effectively, we explore bulk compositions that range from 100% water to 100% hydrogen. It is assumed that there are no bottlenecks preventing water or its dissociation products from reaching the upper atmosphere. Indeed, water condensation is unlikely for the high temperatures expected in the lower atmosphere, which must be consistent with an equilibrium temperature $T_{\rm eq} \sim 1150$ K. Also, separation by mass plays a minor role for the eddy mixing considered here (parameterized through the coefficient $K_{zz} = 10^8$ cm^2 s^{-1}). If a homopause exists, its location can be estimated by equating the eddy and molecular diffusion coefficients of the relevant gases (García Muñoz 2007a). Assuming that these are H and O and a local temperature $\sim T_{\rm eq}$, we estimate that the homopause occurs at $p \sim 0.2$ dyn cm^{-2}. At this level, the bulk velocity of the gas is on the order of m s^{-1}, which is larger than the corresponding eddy or molecular diffusion velocities by 1–2 orders of magnitude. In summary, eddy diffusion ensures that gravitational settling of the heavier gases is inefficient below the $p \sim 1$ dyn cm^{-2} level, and the bulk gas velocity has a similar effect at higher altitudes.

We ran a few preliminary models with various amounts of water prescribed at the lower boundary that revealed that water dissociates very rapidly at the $p = 1$ dyn cm^{-2} level. This is consistent with the findings reported by Guo (2019) for H_2O-rich atmospheres. The leading mechanisms for H_2O reformation in our chemical network are $OH + H_2 \rightarrow H_2O + H$ and $OH + H + H \rightarrow H_2O + H$, that can barely compete with H_2O photolysis (rate coefficient $J_{H_2O} = 2.7 \times 10^{-3}$ s^{-1}). Motivated by this, we opted to prescribe the chemical composition at the lower boundary through the volume mixing ratios (vmrs) of hydrogen ($x_{\rm H}^{\rm LB}$) and oxygen ($x_{\rm O}^{\rm LB}$) atoms, such that $x_{\rm H}^{\rm LB} + x_{\rm O}^{\rm LB} \approx 1$. For all the other gases, we assumed photochemical equilibrium and extrapolated their vmrs from the model cell immediately above the lower boundary. The simulations confirmed that the overall chemistry is driven by the H and O atoms, and that the other gases are much less abundant and rapidly reach equilibrium with them. We explored values of $x_{\rm O}^{\rm LB}$ from 1/3 (i.e., atmospheric

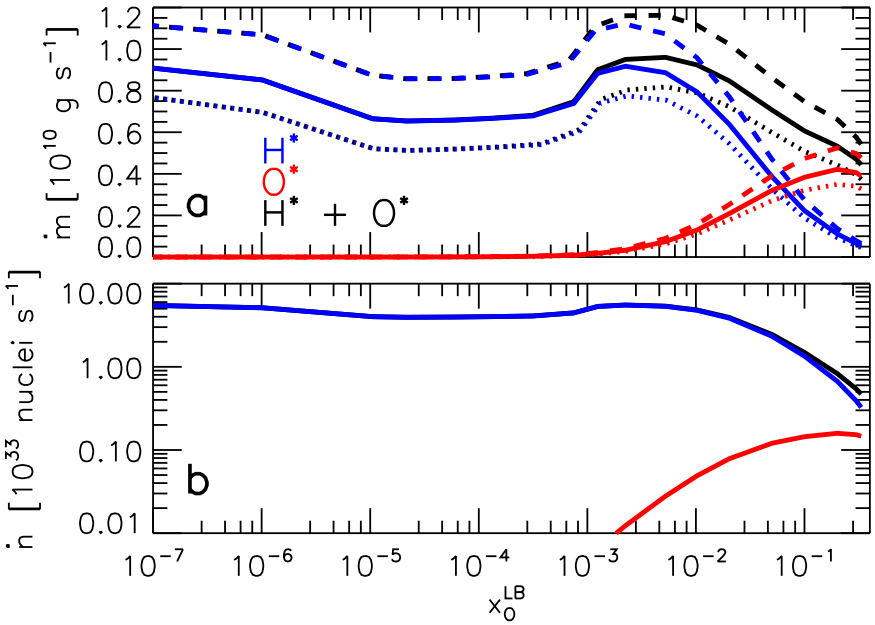

Figure 3. Loss rates for a range of bulk atmospheric compositions as dictated by x_O^{LB} (see text). (a) Mass; (b) Nuclei. In (a) and (b), solid lines correspond to model solutions based on our reference reconstruction of the stellar spectrum. In (a), dashed and dotted lines correspond to solutions for the *high* and *low* stellar spectra, respectively. The loss rates differ by about ±30%, which is consistent with the difference in the integrated X-ray+EUV stellar fluxes.

composition consistent with 100% water) to 0 (i.e., no water in the atmosphere). Or equivalently, x_H^{LB} from 2/3 to 1. For consistency, we normalized all the vmrs at the lower boundary so that their summation is exactly one.

Figure 3(a) shows that the predicted mass loss rates for the whole atmospheric gas are $\dot{m} \sim 4 \times 10^9$–$10^{10}$ g s^{-1} (over a solid angle π) when the reference stellar spectrum is implemented. The mass loss rates are enhanced (diminished) when the *high* (*low*) stellar spectra are implemented, as expected. They are consistent with the 1.2×10^{10} g s^{-1} quoted by Gandolfi et al. (2018) on the basis of the hydrogen-atmosphere models developed by Kubyshkina et al. (2018). These rates are moderately sensitive to the prescribed x_O^{LB} (our proxy for H_2/H_2O partitioning in the bulk atmosphere) even though there is a difference in the gas molecular weight by a factor of up to 6 between models. As expected, the fractionation in the atmosphere between the hydrogen and oxygen atoms is minor. Indeed, the factor $16(\dot{m}_{H^*}/\dot{m}_{O^*})/([H^*]/[O^*])^{LB}$ for the relative loss of hydrogen and oxygen nuclei (H^*, O^*) with respect to their abundances at the lower boundary (brackets stand for number densities) remains in the range 1–1.1 for all cases. In particular, for $x_O^{LB} = 1/3$ we find that $16(\dot{m}_{H^*}/\dot{m}_{O^*})/([H^*]/[O^*])^{LB} \approx 1.1$, which means that the atmosphere loses 2.2 hydrogen nuclei per oxygen nucleus, thereby resulting in its long-term oxidization. A consequence of the moderate variation in $\dot{m}$ between models is that the loss rate of nuclei $\dot{n}$ varies significantly with x_O^{LB}. As x_O^{LB} increases (and therefore the mean molecular weight of the atmosphere increases too), fewer nuclei are lifted off the planet's gravitational potential and the planet develops a less extended atmosphere. Figure 3(b) quantifies the loss rates for H^* and O^* nuclei.

For models with $x_O^{LB} = 0$ (black curves), 2×10^{-2} (red), 10^{-1} (green) and 1/3 (blue), Figures 4(a)–(d) show the profiles of: (a) velocity; (b) temperature; (c) number density of the whole gas and H atoms; (d) number density of O atoms and ionization fractions x_{H^+}/x_H and x_{O^+}/x_O. Velocities ~10 km s^{-1} far from the planet are established in all cases. At any given pressure level the velocities are typically lower when x_O^{LB} is higher (a), which has a direct impact on the temperatures through adiabatic cooling (b). The number density of the whole gas decays more rapidly for the cases with larger x_O^{LB} (c) because in the nearly hydrostatic atmosphere the scale height is smaller for them. This affects how extended the upper atmosphere becomes. The H atom profiles (c) are directly affected by this, but also by how close to the planet the transition between H and H^+ occurs (d). The H^+/H partitioning is controlled by photoionization and the reverse process of radiative recombination, but also by fast charge exchange $H + O^+ \leftrightarrow H^+ + O$ and the fact that O atoms photoionize more readily than H atoms because their cross sections are larger (compare $J_O = 1.7 \times 10^{-4}$ s^{-1} versus $J_H = 5 \times 10^{-5}$ s^{-1} for unattenuated irradiation). Higher abundances of O atoms photoionizing more quickly (and deeper down) than H atoms shift the charge exchange process rightward and push the H^+/H transition closer to the planet. The result is that the H atom profiles (c) are much less extended for higher x_O^{LB}, which has direct implications for their detection. Through charge exchange, the H^+/H and O^+/O ratios follow nearly identical trends (d). Taking the number density [H] = 10^7 cm^{-3} as a reference, this level is reached at $r/R_p \sim 8$, 6.9, 4.4 and 2.6, for the four cases represented in Figures 4(a)–(d) in increasing order by x_O^{LB}. For comparison, if the two processes for charge exchange are artificially switched off in the model for $x_O^{LB} = 1/3$, the level of [H] = 10^7 cm^{-3} shifts from $r/R_p \sim 2.6$ to 3.1. In summary, the assumed bulk composition at the lower boundary of the model has a major impact on how far the H atoms extend. In contrast, for the three cases explored with non-zero x_O^{LB}, the reference level [O] = 10^7 cm^{-3} is reached at $r/R_p \sim 2.2$ (d).

Figures 4(e)–(f) show for $x_O^{LB} = 1/3$ the number densities of various atoms and molecules near the lower boundary (e), and a

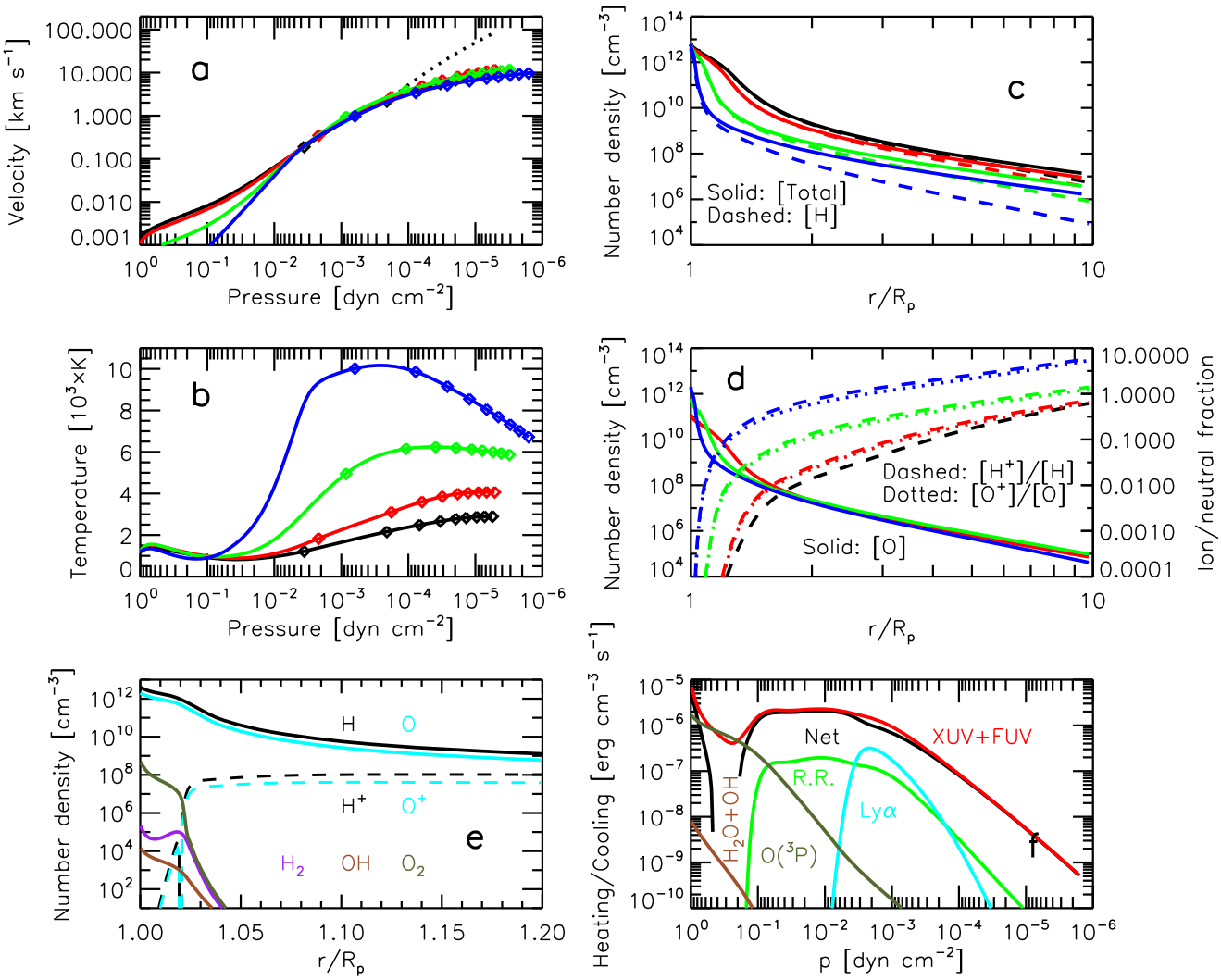

Figure 4. (a)–(d) Various atmospheric profiles for $x_O^{LB} = 0$ (black), 2×10^{-2} (red), 10^{-1} (green) and 1/3 (blue). For $x_O^{LB} = 1/3$: (e) Atmospheric composition near the lower boundary; (f) Radiative contributions to the energy budget: heating by X-ray+EUV+FUV stellar energy deposition; cooling through various emissions (see text). In (a), the black dotted line includes additional gas acceleration (see text) on top of the $x_O^{LB} = 0$ case. In (a) and (b), the symbols mark the locations for $r/R_p = 1.5$, 2.5, 3.5, 4.5, 5.5, 6.5, 7.5, 8.5, and 9.5.

breakdown of the radiative terms that contribute to the energy budget (f). It is interesting to see the spontaneous formation of moderate amounts of O_2 (e), mainly through O+OH→O_2 +H. Both H_2 (shown) and H_2O (not shown, but much less abundant than the other molecules shown) are not readily formed in this oxygen-rich case, which supports our choice of H and O atoms to prescribe the atmospheric composition at the lower boundary. The energy budget over most of the upper atmosphere (f) is dominated by absorption of stellar X-ray +EUV radiation by H and O atoms. At the higher pressures investigated in the model, deposition of stellar FUV energy through the Schumann–Runge bands and continuum of O_2, and O(^3P) cooling through emission at 63 μm also contribute.

4.1. Transit Depths for H and O Atoms

We produced synthetic spectra of H I Lyα absorption at mid-transit to compare with the observations. The absorption is described through a Voigt function with both thermal and natural broadening. The transition wavelengths, probabilities, and oscillator strengths are borrowed from the NIST Bibliographic Database (Kramida 2010; Kramida et al. 2018). It is assumed that the atmospheric profiles of Figure 4 are representative of the entire atmosphere rather than only the substellar direction. The gas escaping toward the star or away from it has a line-of-sight component that Doppler-shifts the absorption line. This is considered by shifting the absorption coefficient in wavelength according to the local line-of-sight velocity, and results in broader absorption spectra. Figure 5(a) shows the transit spectra for H I Lyα absorption based on the models described above (non-brown) together with the spectrum combined from all orbits (uncertainty bars in the measurements have been properly reduced; solid brown) and the reconstructed Lyα line (dashed brown). At the scale of the plot, all four synthetic spectra are undistinguishable because most of the absorption occurs near the Lyα core, which is severely affected by the ISM. In other words, although our model predicts a significant mass loss, the absorption of stellar photons by the escaping atoms based on the predicted velocities overlaps in wavelength with the absorption by the ISM. This difficulty of 1D models such as the one utilized here

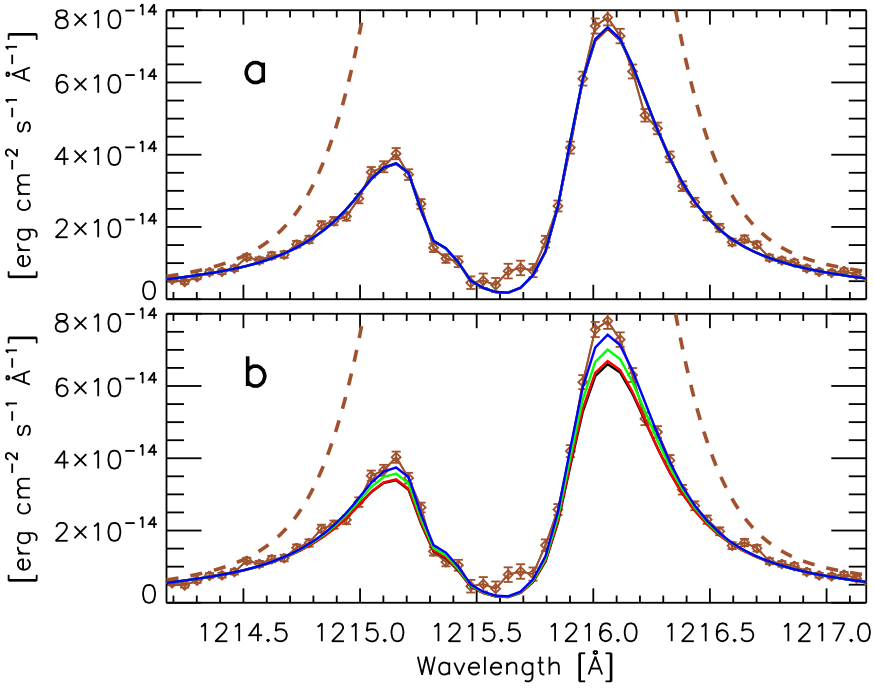

Figure 5. Comparison of the observed spectrum (solid brown) resulting from averaging over all orbits with models. (a) Based on the atmospheric profiles shown in Figure 4. (b) Based on the atmospheric profiles with the $\psi(r/R_p)$ transformation (see the text).

to compare with observations of H I Lyα absorption has long been known.

Indeed, our model does not consider the interaction of the escaping atmosphere with radiation pressure or the stellar wind, which may accelerate the gas faster than the $\sim$10 km s^{-1} seen in Figure 4(a) and enhance the absorption in the Lyα wings (e.g., Tremblin & Chiang 2013; Trammell et al. 2014; Ehrenreich et al. 2015; Bourrier et al. 2018; Shaikhislamov et al. 2018; Debrecht et al. 2019). We explored this issue in an ad hoc manner as follows. Assuming that the mass loss rate is determined below a few planetary radii, and is well predicted by our 1D model, we transformed the velocity and density above that altitude in the way: $u \rightarrow u\psi$, and [H]$\rightarrow$[H]$/\psi$, where $\psi(r/R_p)$ is a function of the radial distance. This transformation lacks a genuine physical basis but at the very least ensures mass conservation if applied to all gases, and enables us to estimate by how much the gas should be accelerated to produce detectable absorption in the Lyα wings. We adopted $\psi(r/R_p < 2.5) \equiv 1$ (no additional acceleration near the planet) and $\psi(r/R_p \geqslant 2.5) = 1+(r/R_p - 2.5)$ (a linear increase in velocity over our hydrodynamic-photochemical model predictions beyond $r/R_p = 2.5$). The resulting spectra, Figure 5(b), show clear differences between model predictions, with the models having smaller x_O^{LB} showing stronger absorption that can be ruled out by our measurements. Unfortunately, our non-detection of H I Lyα absorption cannot distinguish between the scenario of no extra acceleration represented by Figure 5(a) and the scenario of possibly extra acceleration for an atmosphere with significant amounts of oxygen represented by $x_O^{LB} \geqslant 10^{-1}$ in Figure 5(b). Inversely, the exercise confirms that the loss of hydrogen atoms is massive enough in the models with lower x_O^{LB} to produce detectable H I Lyα absorption provided that the atoms are further accelerated at radial distances $r/R_p > 2.5$ to velocities a few times higher than predicted by our 1D model. Such a possibility motivates the current observations of π Men c and future attempts for other small exoplanets.

Absorption by the O I triplet at 1302–1306 Å has been reported for the hot Jupiters HD 209458 b (Vidal-Madjar et al. 2004) and HD 189733 b (Ben-Jaffel & Ballester 2013). We produced O I absorption spectra for π Men c, and found that the transit depths are comparable in our cases with non-zero x_O^{LB}, a finding that simply reflects that the atom number density profiles are similar (Figure 4(d)). The transit depths at the core of the strongest of the triplet components (at 1302 Å), and where the strongest absorption will occur, are on the order of 10% for the standard atmospheric profiles, and 1.5%–2% for the transformed profiles. The drop in the transit depth for the transformed profiles is due to the fact that in this case the line wings absorb comparably to the line core. In practice, an observation that integrated over wavelengths bracketing the line core will result in smaller transit depths than the 10% and 1.5%–2% estimated here.

5. Discussion and Perspective

π Men c is probably one of the best targets to investigate what small exoplanets are made of. Taking the bulk density as a proxy for bulk composition, GJ 436 b ($\rho_p = 1.8$ g cm^{-3}) is the planet most similar to π Men c ($\rho_p = 2.82$ g cm^{-3}) for which H I Lyα absorption has been detected. Loyd et al. (2017) did not find evidence for C II or Si III at GJ 436 b, which suggests that these atoms occur in trace amounts in the atmosphere of

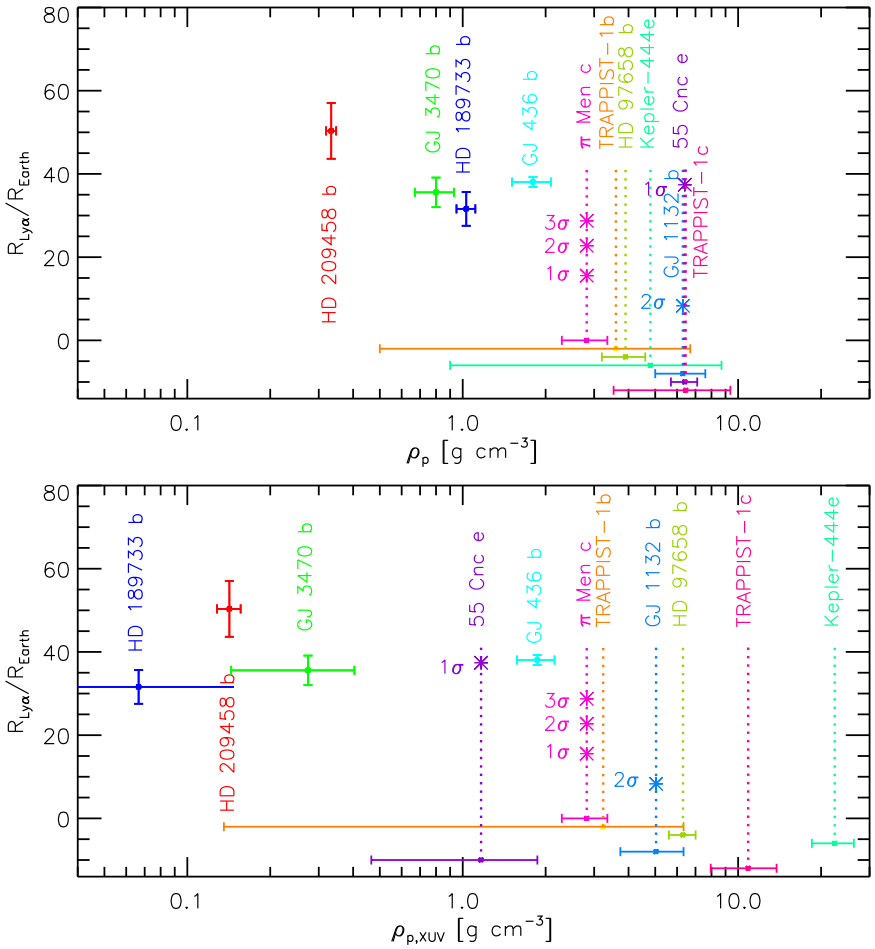

Figure 6. Top panel: for planets for which H I Lyα absorption measurements have been attempted, effective radius at Lyα normalized to Earth's radius vs. planet density. For the four planets with clear detections, $R_{Ly\alpha}/R_\oplus = \sqrt{TD}(R_\star/R_\oplus)$, where TD is the velocity-dependent transit depth quoted in the original references. For the uncertainties in $R_{Ly\alpha}/R_\oplus$, we consider only the 1σ uncertainties in the transit depths. For π Men c and the other more dense planets, the measurements are consistent with no absorption, and we assign an arbitrary $R_{Ly\alpha}/R_\oplus$ <0. We omit error bars for $R_{Ly\alpha}/R_\oplus$ in such cases because they do not necessarily reflect the planet size but other effects such as stellar variability. As exceptions, we show the 1, 2, and 3σ upper limits to $R_{Ly\alpha}/R_\oplus$ for π Men c, the 2σ upper limit for GJ 1132 b, and the 1σ upper limit for 55 Cnc e. Table 2 in Appendix C summarizes the reference sources to prepare this plot. The diagram suggests a transition at 2–3 g cm^{-3} tentatively connected to atmospheric composition. Hydrogen-dominated atmospheres become more extended and easier to detect than non-hydrogen-dominated atmospheres. Among the planets represented here, the transition is bracketed by GJ 436 b and π Men c. Bottom panel: similar to the above, but using the irradiation-corrected density $\rho_{p,XUV}$. In the uncertainties of $\rho_{p,XUV}$, we omit the uncertainties associated with the reconstructed X-ray+EUV stellar flux F_{XUV}. Representing $R_{Ly\alpha}/R_\oplus$ vs. $\rho_{p,XUV}$ generally confirms that less dense planets seem more prone to developing extended atmospheres.

this warm Neptune-sized planet. Using a hydrodynamic-photochemical model similar to ours, they also estimate that GJ 436 b loses mass at a rate of 3.1×10^9 g s^{-1}. This is smaller but comparable to our estimate for π Men c (4×10^9–10^{10} g s^{-1}). Even accounting for the larger stellar size of π Men ($1.1R_\odot$ versus $0.46R_\odot$), it was reasonable to expect that if π Men c's atmosphere is hydrogen-dominated, there would be evidence for an extended atmosphere in our *HST*/STIS measurements. Alternatively, and assuming that the physics implemented in these models is relatively complete, it is fair to argue that our non-detection suggests that π Men c's atmosphere is not hydrogen-dominated. Indeed, our models show that compositions consistent with H_2O, and possibly other heavy molecules such as CO_2 (Tian 2009), will result in reduced number densities of H I in π Men c's upper atmosphere even if the mass loss rate remains high. This occurs also if hydrogen is relatively abundant at the base of the upper atmosphere.

The physics of atmospheric escape is complex, and the planet bulk density is just one of a number of factors that play a role in it. We summarize in Figure 6 previous detections and non-detections of H I Lyα absorption, while looking for a dependence of the measured sizes with the planets' density. In the top panel (effective planet size at Lyα $R_{Ly\alpha}/R_\oplus$ versus planet density ρ_p) π Men c sits between a group of planets for which the atmospheric composition is likely dominated by H_2/He ($\rho_p \leqslant 1.8$ g cm^{-3}) and H I Lyα absorption has been detected, and another group for which other atmospheric compositions with large amounts of heavy molecules are possible ($\rho_p \geqslant 2.8$ g cm^{-3}) and no firm detection of H I Lyα absorption has been reported. The bottom panel is constructed in a similar way, but utilizes instead the irradiation-corrected density $\rho_{p,XUV} = \rho_p(F_{XUV}^{\pi\,Men\,c}/F_{XUV})$ (Appendix C) to account for the theoretical expectation that stronger irradiation potentially compensates for higher planet densities. Both panels are qualitatively consistent and suggest two

different behaviors in the planet sizes at Lyα with a transition at $\rho_p = 2$–$3\ \mathrm{g\ cm^{-3}}$. We propose that Figure 6 may actually reflect a transition in the bulk composition of the planets. Within the transition region, GJ 436 b and π Men c would represent hydrogen-dominated and non-hydrogen-dominated planets, respectively. The case of 55 Cnc e is special because its density ($\rho_p = 6.4\ \mathrm{g\ cm^{-3}}$) is comparatively high, but its irradiation-corrected density is moderately low. Taken at face value from Figure 6, the non-detection of H I Lyα absorption at 55 Cnc e (Ehrenreich et al. 2012) is consistent with the planet lacking an atmosphere (Demory et al. 2016) or having an atmosphere made of heavy molecules (Angelo & Hu 2017).

The idea that Figure 6 shows two separate behaviors can be tested by the search for H I Lyα absorption, but also for O I and C II, in the atmosphere of π Men c and other small exoplanets. In addition, further modeling will help elucidate the specifics of escape for non-hydrogen-dominated atmospheres and the connection between the lower and upper atmospheres, for which little work has been done.

A.G.M. acknowledges support from the DFG priority program SPP 1992 Exploring the Diversity of Extrasolar Planets (grant GA 2557/1–1). A.Y. acknowledges support from STScI grant HST-GO-15699.007.

Appendix A
The Lyα Flux of π Men and Other G Dwarfs

In Figure 7 we compare the Lyα spectrum of π Men with the corresponding spectra of two other G dwarfs, and with the Lyα estimate based on π Men's X-ray flux.

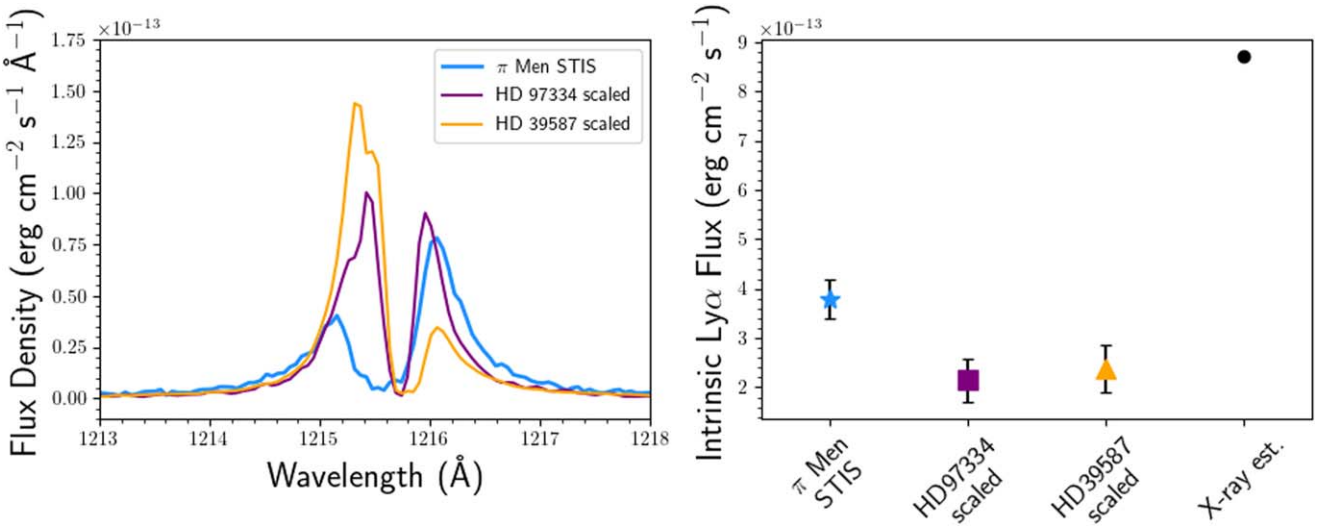

Figure 7. Left panel: the co-added π Men STIS spectrum (blue) is compared to the observed Lyα spectra of two early G dwarfs, HD 97334 (purple) and HD 39587 (orange; Ayres 2010). The two other stars' profiles have been convolved to match π Men's spectral resolution, scaled to match π Men's distance and further scaled down to match π Men's Si III (1206 Å) flux observed with COS (France et al. 2018). Right panel: the reconstructed, intrinsic Lyα flux of π Men from this work is compared to the intrinsic Lyα fluxes of HD 97334 (purple square) and HD 39587 (orange triangle) both from Wood et al. (2005) after applying the same scalings from the left panel. Also shown is the Lyα flux estimate from King et al. (2019) based on π Men's X-ray flux.

Appendix B
Information on the Extraction of the Spectra

In Figure 8 we provide additional information on the extraction of the spectra, and the background and geocoronal emission corrections.

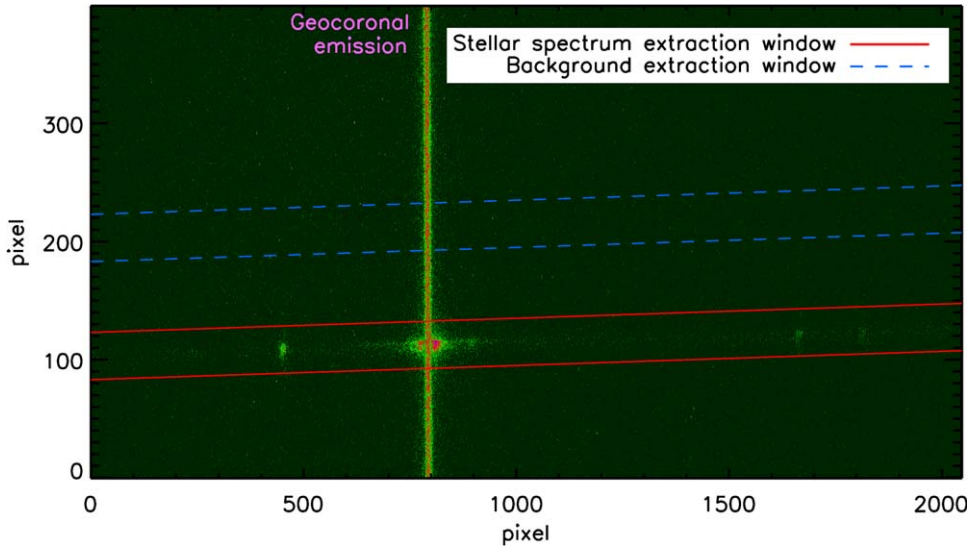

Figure 8. Image of the second *HST* frame in counts per second. The lowest counts are in dark green, while the highest counts are in purple. The vertical line at about 800 pixels along the x-axis is the geocoronal emission. The red solid and blue dashed lines indicate the stellar spectrum and background extraction boxes, respectively. The center of the stellar spectrum extraction box takes the function $103 + 0.012x$, where x is the pixel on the x-axis, and the extraction box has an aperture of 20 pixels, meaning that the total amplitude is of 40 pixels. The background extraction box is identical to the stellar spectrum extraction box, but rigidly shifted upward by 100 pixels.

Appendix C
Exploring Exoplanets' Sizes at Lyα

For energy-limited conditions, the mass loss rate of a planet:

$$\dot{m} \propto \frac{F_{\rm XUV} R_{\rm p}^2}{G M_{\rm p}/R_{\rm p}},$$

where the numerator is the X-ray+EUV irradiation (wavelengths less than 912 Å) received by the planet on its orbit over an effective area $\propto R_{\rm p}^2$, and the denominator is the planet's gravitational potential. $F_{\rm XUV}/\rho_{\rm p}$ is thus a key physical parameter for atmospheric escape.

Based on the above, we define an XUV-corrected planet density:

$$\rho_{\rm p,XUV} = \rho_{\rm p} \frac{F_{\rm XUV}^{\pi\ \rm Men\ c}}{F_{\rm XUV}},$$

which considers simultaneously the planet density and the effect of irradiation on the escape. The choice of the X-ray+EUV irradiation for π Men c as a scaling factor ensures that $\rho_{\rm p,XUV} = \rho_{\rm p}$ for this planet. Table 2 summarizes $\rho_{\rm p}$, $\rho_{\rm p,XUV}$ and $F_{\rm XUV}$ for the sample of planets considered in Figure 6.

Table 2
Data Corresponding to Figure 6

Planet	$\rho_{\rm p}$ (g cm^{-3})	Transit Depth	Reference	$F_{\rm XUV}$ at Planet (erg cm^{-2} s^{-1})	Reference	$\rho_{\rm p,XUV}$ (g cm^{-3})
HD 209458 b	0.33	0.15	Vidal-Madjar et al. (2003)	3162	Louden et al. (2017)	0.14
GJ 3470 b	0.80	0.35	Bourrier et al. (2018)	3938	Bourrier et al. (2018)	0.27
HD 189733 b	1.03	0.14	Lecavelier des Etangs et al. (2012)	20893	Salz et al. (2016)	0.07
GJ 436 b	1.80	0.563	Ehrenreich et al. (2015)	1303	Bourrier et al. (2018)	1.86
π Men c	2.82	⋯	⋯	1350	This work	2.82
TRAPPIST-1b	3.60	⋯	⋯	1502	Bourrier et al. (2017d)	3.23
HD 97658 b	3.90	⋯	⋯	835	Bourrier et al. (2017c)	6.31
Kepler-444e	4.80	⋯	⋯	289	Bourrier et al. (2017b)	22.42
GJ 1132 b	6.30	⋯	⋯	1689†	Waalkes et al. 2019	5.03
55 Cnc e	6.40	⋯	⋯	7413	Salz et al. (2016)	1.16
TRAPPIST-1 c	6.45	⋯	⋯	801	Bourrier et al. (2017d)	10.87

Note. The XUV = X-ray+EUV irradiation is at the planet's orbital position; densities and other information are taken from the NASA Exoplanet Archive (https://exoplanetarchive.ipac.caltech.edu/). †: Estimated from their Equation (6) and quoted mass loss rate 3×10^9 g s^{-1}.

ORCID iDs

A. García Muñoz https://orcid.org/0000-0003-1756-4825
A. Youngblood https://orcid.org/0000-0002-1176-3391
L. Fossati https://orcid.org/0000-0003-4426-9530
D. Gandolfi https://orcid.org/0000-0001-8627-9628
J. Cabrera https://orcid.org/0000-0001-6653-5487

References

Angelo, I., & Hu, R. 2017, AJ, 154, 232
Ayres, T. R. 2010, ApJS, 187, 149
Banks, P. M., & Kockarts, G. 1973, Aeronomy. Part B (New York: Academic)
Batalha, N. M. 2014, PNAS, 111, 12647
Bates, D. R. 1951, PPSB, 64, 805
Ben-Jaffel, L. 2007, ApJL, 671, L61
Ben-Jaffel, L. 2008, ApJ, 688, 1352
Ben-Jaffel, L., & Ballester, G. E. 2013, A&A, 553, A52
Black, J. H. 1981, MNRAS, 197, 553
Bourrier, V., de Wit, J., Bolmont, E., et al. 2017a, AJ, 154, 121
Bourrier, V., Ehrenreich, D., Allart, R., Wyttenbach, A., & Semaan, T. 2017b, A&A, 602, A106
Bourrier, V., Ehrenreich, D., King, G., et al. 2017c, A&A, 597, A26
Bourrier, V., Ehrenreich, D., Wheatley, P. J., et al. 2017d, A&A Letters, 599, L3
Bourrier, V., Lecavelier des Etangs, A., Dupuy, H., et al. 2013, A&A, 551, A63
Bourrier, V., Lecavelier des Etangs, A., Ehrenreich, D., et al. 2018, A&A, 620, A147
Chassefière, E. 1996, JGR, 101, 26039
Debrecht, A., Carroll-Nellenback, J., Frank, A., et al. 2019, MNRAS, 483, 1481
Demory, B.-O., Gillon, M., de Wit, J., et al. 2016, Natur, 532, 207
Ehrenreich, D., Bourrier, V., Bonfils, X., et al. 2012, A&A, 547, A18
Ehrenreich, D., Bourrier, V., Wheatley, P. J., Lecavelier des Etangs, A., & Hébrard, G. 2015, Natur, 522, 459
Fortier., A., Beck, T., Benz, W., et al. 2014, Proc. SPIE, 9143, 91432J
France, K., Arulanantham, N., Fossati, L., et al. 2018, ApJS, 239, 16
Fulton, B. J., Petigura, E. A., Howard, A. W., et al. 2017, AJ, 154, 109
Gaia Collaboration, Brown, A. G. A., Vallenari, A., et al. 2018, A&A, 616, A1
Gandolfi, D., Barragán, O., Livingston, J. H., et al. 2018, A&AL, 619, L10
García Muñoz, A. 2007a, P&SS, 55, 1414
García Muñoz, A. 2007b, P&SS, 55, 1426
García Muñoz, A., McConnell, J. C., McDade, I. C., & Melo, S. M. L 2005, Icar, 176, 75
García Muñoz, A., & Schneider, P. C. 2019, ApJL, 884, L43
Guo, J. H. 2019, ApJ, 872, 99
Hollenbach, D., & McKee, C. F. 1979, ApJS, 41, 555
Huang, C. X., Burt, J., Vanderburg, A., et al. 2018, ApJL, 868, L39
Johnstone, C. P., Güdel, M., Lammer, H., & Kislyakova, K. G. 2018, A&A, 617, A107
Jones, H. R. A., Butler, R. P., Tinney, C. G., et al. 2002, MNRAS, 333, 871
Kasting, J. F., & Pollack, J. B. 1983, Icar, 53, 479
King, G. W., Wheatley, P. J., Bourrier, V., & Ehrenreich, D. 2019, MNRAS, 484, L49
Kramida, A. 2010, Atomic Energy Levels and Spectra Bibliographic Database (version 2.0), https://physics.nist.gov
Kramida, A., Ralchenko, Yu., Reader, J. & NIST ASD Team 2018, NIST Atomic Spectra Database (ver. 5.5.6), https://physics.nist.gov/asd
Kreidberg, L. 2015, PASP, 127, 1161
Kubyshkina, D., Fossati, L., Erkaev, N. V., et al. 2018, A&A, 619, A151
Kulow, J. R., France, K., Linsky, J., & Loyd, R. O. P. 2014, ApJ, 786, 132
Lecavelier des Etangs, A., Bourrier, V., Wheatley, P. J., et al. 2012, A&A, 543, L4
Lecavelier des Etangs, A., Ehrenreich, D., Vidal-Madjar, A., et al. 2010, A&A, 514, A72
Lopez, E. D., & Fortney, J. J. 2013, ApJ, 776, 2
Louden, T., Wheatley, P. J., & Briggs, K. 2017, MNRAS, 464, 2396
Loyd, R. O. P., Koskinen, T. T., France, K., Schneider, C., & Redfield, S. 2017, ApJL, 834, L17
Marcy, G. W., Weiss, L. M., Petigura, E. A., et al. 2014, PNAS, 111, 12655
Miller, S., Stallard, T., Tennyson, J., & Melin, H. 2013, JPCA, 117, 9770
Owen, J. E., & Wu, Y. 2013, ApJ, 775, 105
Pickles, A. J. 1998, PASP, 110, 863
Rauer, H., Catala, C., Aerts, C., et al. 2014, ExA, 38, 249
Redfield, S., & Linsky, J. L. 2008, ApJ, 673, 283
Ricker, G. R., Winn, J. N., Vanderspek, R., et al. 2015, JATIS, 1, 014003
Rogers, L. A. 2015, ApJ, 801, 41
Salz, M., Czesla, S., Schneider, P. C., & Schmitt, J. H. M. M. 2016, A&A, 586, A75
Shaikhislamov, I. F., Khodachenko, M. L., Lammer, H., et al. 2018, MNRAS, 481, 5315
Tian, F. 2009, ApJ, 703, 905
Tian, F., Kasting, J. F., Liu, H.-L., & Roble, R. G. 2008, JGRE, 113, E05008
Trammell, G. B., Li, Z.-Y., & Arras, P. 2014, ApJ, 788, 161
Tremblin, P., & Chiang, E. 2013, MNRAS, 428, 2565
Valencia, D., Guillot, T., Parmentier, V., & Freedman, R. S. 2013, ApJ, 775, 10
Van Eylen, V., Agentoft, C., Lundkvist, M. S., et al. 2018, MNRAS, 479, 4786
Vidal-Madjar, A., Désert, J.-M., Lecavelier des Etangs, A., et al. 2004, ApJL, 604, L6
Vidal-Madjar, A., Lecavelier des Etangs, A., Désert, J.-M., et al. 2003, Natur, 422, 143
Waalkes, W. C., Berta-Thompson, Z., Bourrier, V., et al. 2019, AJ, 158, 50
Wood, B. E., Redfield, S., Linsky, J. L., Müller, H.-R., & Zank, G. P. 2005, ApJ, 159, 118
Woods, T. N., Chamberlin, P. C., Harder, J. W., Hock, R. A., & Snow, M. 2009, GeoRL, 36, L01101
Youngblood, A., France, K., Loyd, R. O., et al. 2016, ApJ, 824, 101
Zahnle, K. J., & Kasting, J. F. 1986, Icar, 68, 462